Orbital order and partial electronic delocalization in a triangular magnetic metal Ag_2MnO_2

S. Ji,[1] E. J. Kan,[2] M.-H. Whangbo,[2] J.-H. Kim,[1] Y. Qiu,[3] M. Matsuda,[4] H. Yoshida,[5] Z. Hiroi,[5] M. A. Green,[3] T. Ziman,[6] and S.-H. Lee[1,*]

[1]*Department of Physics, University of Virginia, Charlottesville, Virginia 22904-4714, USA*

[2]*Department of Chemistry, North Carolina State University, Raleigh, North Carolina 27695-8204, USA*

[3]*NIST Center for Neutron Research, National Institute of Standards and Technology, Gaithersburg, Maryland 20899, USA*

[4]*Quantum Beam Science Directorate, Japan Atomic Energy Agency (JAEA), Tokai, Ibaraki 319-1195, Japan*

[5]*Institute for Solid State Physics, University of Tokyo, Kashiwa, Chiba 277-8581, Japan*

[6]*Institut Laue Langevin, Boite Postale 156, F-38042 Grenoble Cedex 9, France*

(Received 12 February 2010; revised manuscript received 1 March 2010; published 18 March 2010)

Magnetic and electrical properties of Ag_2MnO_2 were examined by elastic and inelastic neutron-scattering measurements and by density-functional calculations. The spins of the triangular antiferromagnet metal Ag_2MnO_2 are found to freeze into a gapless short-range collinear state below 50 K because of a ferro-orbital ordering and spin-orbit coupling of the high-spin Mn^{3+} ions. The decrease in the spin-spin correlation lengths of Ag_2MnO_2 in the order, $\xi_b \gg \xi_a \gg \xi_c$, is explained by the spin-exchange interactions calculated for the ferro-orbital ordered state. The electronic states around the Fermi level have significant contributions from the spin-polarized Mn $3d$ and O $2p$ states, which makes electron-electron scattering dominate over electron-phonon scattering at low temperatures leading to the $\rho \propto T^2$ behavior below 50 K.

DOI: 10.1103/PhysRevB.81.094421 PACS number(s): 75.25.−j, 61.05.cp, 61.05.fm, 75.50.Ee

I. INTRODUCTION

Unconventional collective behaviors often arise when electron-electron Coulomb repulsion is neither strong (leading to electron localization and magnetism) nor weak (leading to electron delocalization and metallicity). A well-known example is the high-temperature superconductivity found in cuprates and iron superconductors.[1,2] Other materials also exhibit unusual low-temperature behaviors arising from the competition between the metallicity and magnetism. An example is Ag_2MO_2 (M=Mn,Ni) in which magnetic MnO_2 layers alternate with metallic Ag_2 double layers along the c axis.[3,4] Bulk magnetic susceptibility follows the Curie-Weiss law for localized moments at high temperatures while resistivity exhibits metallic behaviors at low temperatures. It has been thought that the metallic property arises from the Ag $5s$ electrons of the $(Ag_2)^+$ layers while the magnetic property from the Mn $3d$ electrons of the high-spin $Mn^{3+}(t_{2g}^3 e_g^1)$ ions in the MnO_2 layers. At low temperatures (T), the resistivity ρ of a metal dominated by the electron-phonon scattering process is expected to be proportional to T^5. However, the ρ of Ag_2MnO_2 is proportional to T^2, and such behavior is expected for a Fermi liquid with large electron correlations. Furthermore, the coefficient of the T^2 term, $A=2.86\times10^{-4}$ $\mu\Omega$ cm K^{-2}, is much larger than expected if only the Ag electrons are involved in the transport process.[3,4] One might expect frustrated magnetic interactions in Ag_2MnO_2 because the Mn^{3+} ions form a triangular lattice in the ab plane. Despite the presence of strong antiferromagnetic interactions, evidenced by the large Curie-Weiss temperature, $\Theta_{CW}=-400$ K, Ag_2MnO_2 does not exhibit any long-range-order (LRO) down to $T_g=22$ K, at which specific heat and bulk susceptibility data show a spin-glassy order.[4] In contrast, Ag_2NiO_2 has much weaker antiferromagnetic interactions ($\Theta_{CW}=-33$ K) but shows a LRO below $T_N=56$.[3]

In this work, we explore the apparently puzzling electrical and magnetic properties of Ag_2MnO_2 by elastic/inelastic neutron-scattering measurements on a powder sample of Ag_2MnO_2 and also by density-functional calculations. Our study shows that the ferro-orbital ordering of the high-spin Mn^{3+} ions in Ag_2MnO_2, which takes place below 540 K, is responsible for the puzzling magnetic properties of Ag_2MnO_2 at low temperatures. The Mn^{3+} electrons are partially delocalized, thereby leading to the T^2 behavior with a large effective mass of the itinerant electrons in the resistivity measurements.

II. EXPERIMENT

A 2 g powder sample of Ag_2MnO_2 was prepared at the ISSP of the University of Tokyo using the solid-state reaction technique with stoichiometric mixture of Ag and MnO_2 powder.[4] A series of neutron-scattering measurements were performed at the NIST Center for Neutron Research (NCNR). Time-of-flight neutron-scattering measurements were carried out using the disk chopper spectrometer (DCS) with wavelengths of $\lambda=1.8$, 2.9, and 4.8 Å. Neutron powder-diffraction (NPD) measurements were performed on the BT1 powder diffractormeter with a Cu(311) monochromator ($\lambda=1.5403$ Å), and Rietvelt refinement was carried out using FULLPROF program.[5] Temperature dependence of the nuclear Bragg peaks was studied at TAS-2 located at the JRR-3 with 14.7 meV incident neutrons and horizontal collimations of guide-80′-80′-40′. Density-functional calculations for the low-temperature monoclinic phase of Ag_2MnO_2 employed the projector-augmented wave method[6] encoded in the Vienna *ab initio* simulation package,[7,8] the PW91 functional form[9] of the generalized gradient approximation (GGA), and the plane-wave cutoff energy of 400 eV. The GGA plus on-site repulsion U method (GGA+U) was employed to properly describe the electron correlation associ-

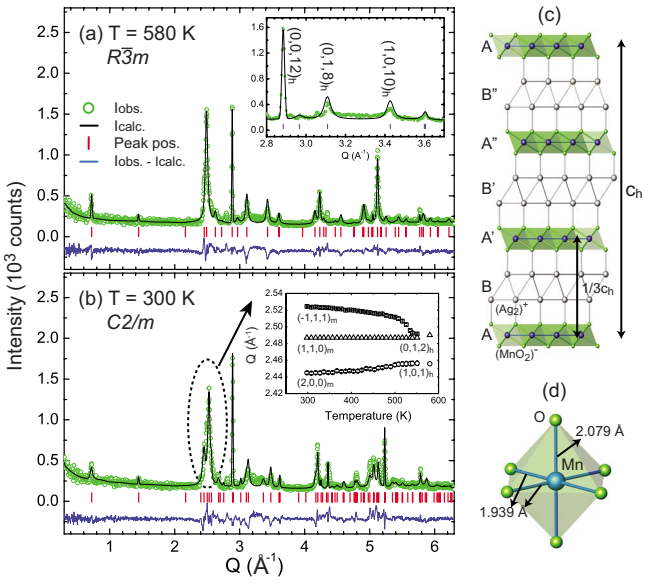

FIG. 1. (Color online) Neutron powder-diffraction data measured (a) at 580 K and (b) 300 K. Circles are the data and the line represents the calculated intensity based on the lattice parameters listed in Table I. The inset of (a) shows a closeup of a narrow range of wave vector Q while the inset of (b) shows the monoclinic splitting of the two peaks around $Q \sim 2.5$ Å^{-1} into three peaks below 540 K. (c) The stacking of the MnO_2 and Ag layers along the c axis in the high-temperature trigonal phase. (d) The local Jahn-Teller distortion of the MnO_6 octahedra in the MnO_2 layer.

ated with the Mn $3d$ states[10] with $U=2.5$ and 4.5 eV. The spin-exchange interactions of Ag_2MnO_2 were evaluated by performing seven ordered spin states of the $(2a,4b,2c)$ magnetic supercell, with a set of $2\times7\times4$ k points for the irreducible Brillouin zone.

III. RESULTS

A. Neutron diffraction and crystal structure

As shown in Fig. 1(a), at 580 K, the nuclear Bragg reflection positions tell us that the high-temperature crystal structure is trigonal with $R\bar{3}m$ symmetry. The $(0,0,L)$ reflections are instrument resolution limited but the (H,K,L) reflections with nonzero H or K are much broader than the Q resolution. This broadening was well fit by including stacking disorder along the c axis. The best fit, shown as the solid line, was obtained with the lattice parameters listed in Table I and the stacking correlation length of 217(37) Å. As depicted in Fig. 1(c), the chemical unit cell of the perfect hexagonal structure consists of MnO_2 layers (A, A′, and A″) alternating with Ag bilayers (B, B′, and B″). Adjacent MnO_2 layers are displaced by (1/3,1/3,1/3), and so are adjacent Ag bilayers. The stacking faults may occur due to weak Ag-O interactions between every Ag bilayer and its neighboring MnO_2 layers [see Fig. 1(c)]. Thus, the stacking order of the layers can be imperfect, instead of the long-range stacking of A-B-A′-B′-A″-B″ one might expect for a perfect crystal, stacking faults such as A-B-A′-B″-A″-B′ or A-B″-A″-B-A′-B′ may occur. Such stacking faults will not change the c positions of the layers but disorder the arrangements of the ab positions of the atoms along the c axis, and yield the observed broadenings of the $(H\neq0,K\neq0,L)$ nuclear Bragg reflections as shown in the inset of Fig. 1(a).

TABLE I. The crystal structural parameters of Ag_2MnO_2 obtained at 580 and 300 K by refining the data shown in Fig. 1 using the program FULLPROF. B_{iso} is an isotropic thermal parameter expressed as $\exp(-B_{iso}\sin^2\theta/\lambda^2)$, where θ is the scattering angle and λ is the wavelength of the neutron.

580 K($R\bar{3}m$), $\chi^2=3.92$, $R_{F^2}=12.1$, $R_{wp}=12.6$, $a=b=2.9699(2)$ Å, $c=26.140(2)$ Å

Atom(W)	x	y	z	B_{iso} (Å^2)
Ag ($6c$)	0	0	0.2106(2)	1.4(2)
Mn ($3a$)	0	0	0	1.7(3)
O ($6c$)	0	0	0.2955(3)	3.3(2)

Mn-O=1.9831(4) Å

300 K($C2/m$), $\chi^2=5.48$, $R_{F^2}=15.0$, $R_{wp}=14.7$, $a=5.2472(6)$ Å, $b=2.8823(2)$ Å, $c=8.899(1)$ Å, $\beta=102.4(1)°$

Atom(W)	x	y	z	B_{iso} (Å^2)
Ag ($4i$)	0.212(2)	0	0.6288(7)	0.8(2)
Mn ($2a$)	0	0	0	1.1(3)
O ($4i$)	0.304(2)	0	0.8833(9)	2.8(2)

Mn-O(apical)=2.079(6) Å, Mn-O(plane)=1.939(2) Å

Upon cooling from 580 K, the two Bragg reflections over $2.4<Q<2.6$ Å^{-1} split into five peaks at ~540 K, indicating that the crystal symmetry is lowered [see the inset of Fig. 1(b)]. The best refinement of the NPD data taken at 300 K [Fig. 1(b)] was obtained with a monoclinic $C2/m$ crystal structure with the lattice parameters listed in Table I. The symmetry lowering is due to the Jahn-Teller distortion of each MnO_6 octahedron, which involves an axial elongation of every MnO_6 octahedron along the direction close to the a axis, as shown in Fig. 1(d). As a result of this ferro-orbital order, the e_g electron of every high-spin Mn^{3+} ion occupies the $d_{3r^2-z^2}$ orbital (with the local z axis of each MnO_6 octahedron along the elongated O-Mn-O bonds).

B. Neutron scattering and magnetic correlations

Figures 2(a)–2(c) show the neutron-scattering intensity obtained at DCS as a function of the momentum (Q) and the energy ($\hbar\omega$) transfer, measured at $T=80$, 40, and 1.4 K. At 80 K $\gg T_g$, $S(\boldsymbol{Q},\omega)$ exhibits a broad continuum over $\hbar\omega$. The Q dependence of the low-energy continuum is asymmetric with a sharp increase at $Q\simeq1.25$ Å^{-1} and a broad tail at higher Q. This indicates that the spin fluctuations are low-dimensional in nature. Figure 2(d) shows T dependence of the low-energy fluctuations $S(\omega)=\int_{1\text{ Å}^{-1}}^{2\text{ Å}^{-1}} S(Q,\omega)dQ$ obtained from the $\lambda=4.8$ Å data with an instrumental energy resolution of $\Delta E=0.11$ meV. Upon cooling from 120 K, the low-energy spin fluctuations increase and become strongest at 60 K below which they weaken. Figure 2(e) shows that the nominally static spin correlations with lifetime longer than $\Delta\tau_{min}\simeq\frac{\hbar}{\Delta E}\simeq3.29$ ps develop below T_f, which is higher than $T_g=22$ K determined by the bulk susceptibility measure-

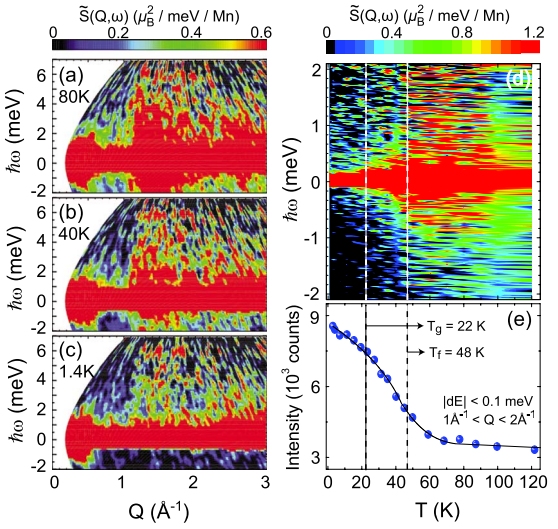

FIG. 2. (Color online) (a)–(c) Color contour maps of neutron-scattering intensity as a function of wave vector, Q, and energy transfer, $\hbar\omega$, measured with $\lambda=2.4$ Å at (a) 80 K, (b) 40 K, and (c) 1.4 K. (d) $\hbar\omega$ dependence of low-energy spin fluctuations measured with $\lambda=4.9$ Å at various temperatures spanning the phase transition. (e) T dependence of the elastic magnetic intensity obtained by the neutron intensity over $1<Q<2$ Å^{-1} and $|dE|<0.1$ meV. T_f was determined from Fig. 4(d).

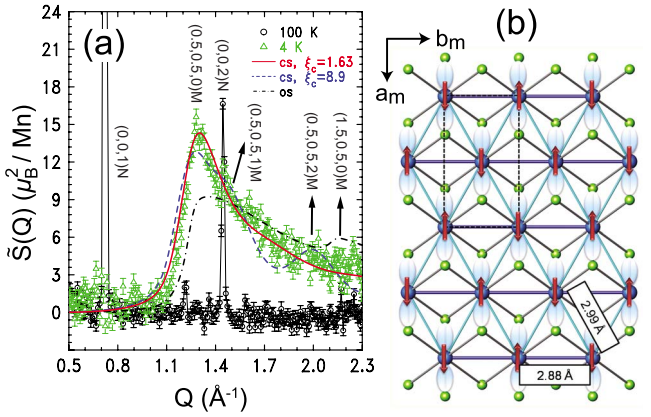

FIG. 3. (Color online) (a) Elastic neutron-scattering intensity, $\tilde{I}(Q)$, at 4 and 100 K. For 4 K$<T_f$, nonmagnetic background measured at 100 K was subtracted to get magnetic contributions only. The reflection indices are in the monoclinic notations. The lines are described in the text. (b) ab projection of the MnO_2 triangular layer with a magnetic structure that is consistent with the characteristic wave vector, $\boldsymbol{q}_m=(0.5,0.5,0)_{\text{mono}}$, of $\tilde{I}(Q)$. The bigger and smaller spheres are Mn and O ions, respectively. The ovals represent the $d_{3r^2-z^2}$ orbitals with the local z axis along the axially elongated O-Mn-O bonds. The thick (thin) blue lines refer to the short (long) bonds between neighboring Mn ions. The dotted lines represent the chemical unit cell of the monoclinic phase.

ments with $\Delta E=0$. Detecting different transition temperatures with different energy resolutions is common for magnetic systems such as spin glasses where spins freeze into a short-range ordered state.[11–13]

To gain insight into the nature of static short-range magnetic order below T_f, we plot the Q dependence of the elastic-scattering intensity obtained by integrating the $\lambda=4.8$ Å data over an energy window of $|\hbar\omega|<0.2$ meV. Figure 3(a) shows the resulting $S(Q)$ at $T=4$ and 100 K. The 100 K ($>T_f$) data were taken as the nonmagnetic background and were subtracted from the other T data. The resulting magnetic $S(Q)$ exhibits a broad peak without any magnetic Bragg peaks, indicating that the static spin correlations are short ranged. The broad peak is located at $Q=1.251$ Å^{-1} that corresponds to a characteristic wave vector of $\boldsymbol{q}_m=(0.5,0.5,0)$. Furthermore, the elastic $S(Q)$ is asymmetric as the low-energy excitations are shown in Figs. 2(a)–2(c), indicating that the short-range magnetic ordered structure is low dimensional. For a quantitative analysis, we fit $S(Q)$ to the elastic neutron cross section described by the product of the independent lattice-Lorentzian functions,[14]

$$\frac{d\sigma_{el}}{d\Omega}(\boldsymbol{Q}) \propto |F_m^{\perp}(\boldsymbol{Q})|^2 \prod_{\alpha} \frac{\sinh \xi_{\alpha}^{-1}}{\cosh \xi_{\alpha}^{-1} - \cos[(\boldsymbol{q}_m - \boldsymbol{Q}) \cdot \boldsymbol{r}_{\alpha}]}. \tag{1}$$

Here $F_m^{\perp}(\boldsymbol{Q})$, the unit-cell magnetic structure factor normal to the scattering vector, can be written as $F_m^{\perp}(\boldsymbol{Q})=f(Q)^2\Sigma_{\nu}\boldsymbol{M}_{\nu}^{\perp}e^{-i\boldsymbol{Q}\cdot\boldsymbol{r}_{\nu}}$, where $\boldsymbol{M}_{\nu}$ and $\boldsymbol{r}_{\nu}$ are the staggered magnetic moment and the position of an Mn^{3+} ion at the site ν, respectively, and $f(Q)$ is the Mn^{3+} magnetic form factor. ξ_{α} and $\hat{\boldsymbol{r}}_{\alpha}$ are the spin-correlation length and the unit lattice vector along the α axis, respectively.

Two spin structures that have the characteristic wave vector of $\boldsymbol{q}_m=(0.5,0.5,0)$ are considered: a collinear spin structure (CS) where antiferromagnetic (AFM) chains are formed along the b axis as shown in Fig. 3(b), and an orthogonal spin structure (OS) where the spin directions of the neighboring AFM chains along the a axis are orthogonal. It is straightforward to compare the two models because they give different ratios of the structure factors for the two magnetic reflections, (1/2,1/2,0) and (3/2,1/2,0). The magnetic structure factor for the two models can be written as

$$F_m(\text{CS}) \propto \Phi \times (1 - e^{\pi i(H+K)}),$$

$$F_m(\text{OS}) \propto \Phi \times (\hat{\boldsymbol{a}} - e^{\pi i(H+K)}\hat{\boldsymbol{b}}), \tag{2}$$

where $\Phi=1-e^{2\pi iH}-e^{2\pi iK}+e^{2\pi i(H+K)}$, and $\hat{\boldsymbol{a}}$ and $\hat{\boldsymbol{b}}$ are the unit vectors along the a and b axes. Thus, the ratio of $\frac{F_m(3/2,1/2,0)}{F_m(1/2,1/2,0)}$ is 0 for the CS case while it is 1 for the OS case. As a result, the OS model would produce a prominent peak at $Q\simeq 2.17$ Å^{-1} that corresponds to the (3/2,1/2,0) reflection, which is inconsistent with the data as shown as the black dashed dotted line in Fig. 3(a). Thus, we conclude that the spin freezing in Ag_2MnO_2 occurs in the form of the collinear spin structure. The red solid line in Fig. 3(a) is the best fit obtained with the collinear spin structure and the correlation lengths of $\xi_b=18.9(37)$ Å along the chain, $\xi_a=5.9(18)$ Å perpendicular to the chain in the triangular plane, and a negligible out-of-plane correlation length of $\xi_c=1.6(16)$ Å. For comparison, we also show the calculated $S(Q)$ of a collinear spin structure obtained with the same ξ_a and ξ_b but ξ_c to be

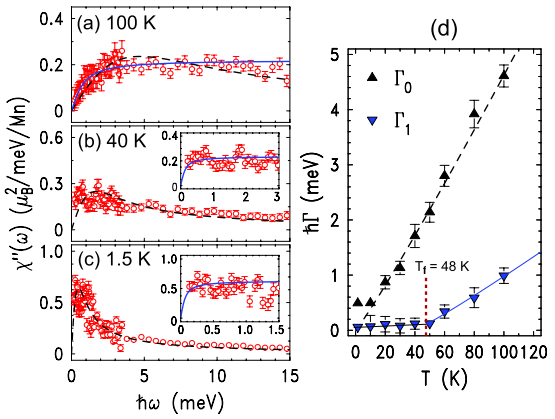

FIG. 4. (Color online) (a)–(c) Energy dependence of the imaginary part of the dynamic susceptibility, $\chi''(\omega)$, obtained by integrating and converting the inelastic neutron-scattering intensity $I(Q,\omega)$ shown in Fig. 2 over $1<Q<2$ Å^{-1} at (a) 100 K, (b) 40 K, and (c) 1.5 K. Dashed lines (black) and solid lines (blue) represent fits by spectral weight functions of Lorentzian type and arctan which give linewidths (Γ_0) and the lower limit (Γ_1) of spin-relaxation rates, respectively. (d) Spin-relaxation rates as a function of temperature. Lines are described in the text.

the interlayer distance between the neighboring triangular layers, 8.9 Å (see the blue dashed line), which does not reproduce the data. The fact that $\xi_b \gg \xi_a \gg \xi_c$ indicates that the magnetic interactions in Ag_2MnO_2 are quasi-one-dimensional.

Let us now turn to the nature of the dynamical spin correlations. We obtained energy dependence of the scattering intensity, $I(\omega)$, by integrating all $I(Q,\omega)$ data taken with $\lambda=1.8$, 2.8, and 4.9 Å over $1<Q<2$ Å^{-1}. Then, using the detailed balance relation $\chi''(\omega)=\frac{\pi}{3}(1-\exp^{-\hbar\omega/k_BT})I(\omega)$, where k_B is the Boltzmann constant and the imaginary part of the dynamic susceptibility, χ'', was extracted. As shown in Fig. 4(a), at $T_f<100$ K$\ll|\Theta_{CW}|$, $\chi''(\omega)$ can be well fitted to a Lorentzian-type function, $\chi''(\omega)\propto\Gamma_0\omega/(\Gamma_0^2+\omega^2)$. When the temperature decreases, however, the spectral weight shifts down to lower energies and the Lorentzian-type function cannot reproduce the low-energy region while it fits the higher-energy region. Below T_f, the low-energy region can be fitted to $\chi''(\omega)\propto\tan^{-1}(\omega/\Gamma_1)$, which represents spin relaxations with a distribution of the relaxation rates with the lower limit being Γ_1.[11] The optimal relaxation rates are plotted in Fig. 4(d). For $T>T_g$, the overall relaxation rate is obtained by fitting to a power-law function of $\Gamma_0=C_0(k_BT)^{\alpha_0}$ with $C_0=0.5(1)$ and $\alpha_0=1.08(16)$ displayed with a dashed line. For $T>T_f$, the relaxation rate of the lower limit (a solid line) $\Gamma_1=C_1(k_BT)^{\alpha_1}$ with $C_1=0.18(6)$ and $\alpha_1=1.07(16)$. For $T<T_f$, $\Gamma_1=0.11(2)$ meV, which is almost zero, independent of temperature. This contrasts with the behavior of Γ found in a well-known quasi-two-dimensional system $SrCr_{9p}Ga_{12-9p}O_{19}$ (SCGO) in which the magnetic Cr^{3+} ions form a [111] slab of a three-dimensional network of corner-sharing tetrahedra:[15] upon cooling above T_f, the Γ of SCGO decreases linearly to zero at T_f. Upon further cooling, however, it increases back. This observation was attributed to the absence of local low-energy excitations in the frozen state.[12]

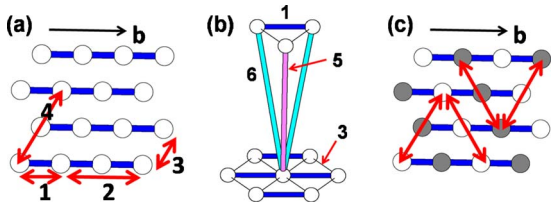

FIG. 5. (Color online) The spin-exchange paths of Ag_2MnO_2 (a) within the MnO_2 layer and (b) between adjacent MnO_2 layers. The circles represent the Mn^{3+} ions, and the numbers 1–6 refer to the spin exchanges J_1–J_6, respectively. (c) The spin arrangement in the MnO_2 layer showing that the NNN interchain interactions are not frustrated. The arrows represent some ferromagnetic J_4 interactions

C. Spin exchanges and magnetic properties

To account for the magnetic properties of Ag_2MnO_2 observed from the neutron-scattering study presented in the previous section, it is necessary to estimate the values of its spin-exchange parameters J_1–J_6 defined in Figs. 5(a) and 5(b). For this purpose, we perform GGA+U calculations for seven ordered spin states (FM and AF1–AF6) depicted in Fig. 6 in terms of the $(2a,4b,2c)$ magnetic supercell, i.e., 32 formula units (FUs). The relative energies of these states (in millielectron volt per 32 FUs) are summarized in Fig. 6. Given the spin Hamiltonian,

$$H=-\sum_{i<j}J_{ij}\boldsymbol{S}_i\cdot\boldsymbol{S}_j, \tag{3}$$

where $\boldsymbol{S}_i$ and $\boldsymbol{S}_j$ are the spin operators at the spin sites i and j, respectively, and $J_{ij}(=J_1$–$J_6)$, the total spin-exchange interaction energies of the FM and AF1–AF6 states (per 32

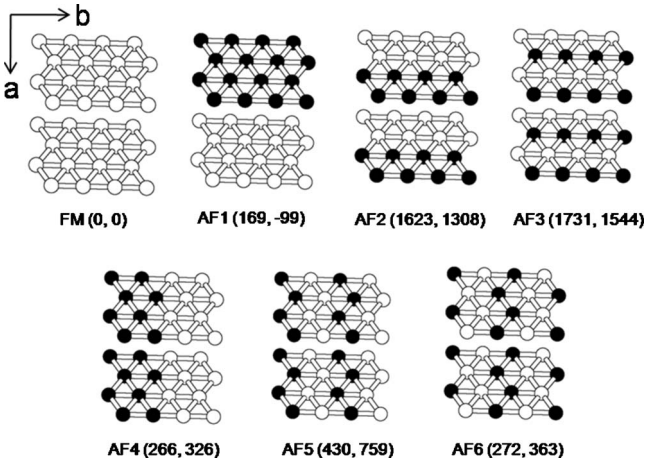

FIG. 6. The ordered spin states, defined in terms of the $(2a,4b,2c)$ magnetic supercell, used to extract the spin-exchange parameters J_1–J_6 by GGA+U calculations with $U=2.5$ and 4.5 eV. Only the Mn^{3+} ions of two MnO_2 layers are shown, and the unshaded and shaded circles represent the Mn^{3+} ions with up and down spins, respectively. The relative energies (in millielectron volt per 32 FUs) of the seven ordered spin states are given in parentheses, where the first and second numbers refer to the relative energies with respect to the FM state obtained with $U=2.5$ and 4.5 eV, respectively.

TABLE II. The values of the spin-exchange parameters J_1-J_6 (in meV) obtained from GGA+U calculations with $U=2.5$ and 4.5 eV.

	$U=2.5$ eV	$U=4.5$ eV
J_1	−4.66	−2.41
J_2	−0.18	0.18
J_3	2.75	3.55
J_4	1.50	1.05
J_5	−0.61	0.67
J_6	0.65	−0.53

FUs) are obtained as summarized below by applying the energy expressions obtained for spin dimers with N unpaired spins per spin site (in the present case, $N=4$ and H's are normalized by $N^2/4$),[16,17]

$$H_{\mathrm{FM}} = -32J_1 - 32J_2 - 64J_3 - 64J_4 - 32J_5 - 64J_6,$$

$$H_{\mathrm{AF1}} = -32J_1 - 32J_2 - 64J_3 - 64J_4 + 32J_5 + 64J_6,$$

$$H_{\mathrm{AF2}} = -32J_1 - 32J_2 + 64J_4 - 32J_5,$$

$$H_{\mathrm{AF3}} = -32J_1 - 32J_2 + 64J_3 - 64J_4 - 32J_5 + 64J_6,$$

$$H_{\mathrm{AF4}} = +32J_2 - 32J_3 - 32J_5 - 32J_6,$$

$$H_{\mathrm{AF5}} = +32J_1 - 32J_2 + 64J_4 - 32J_5,$$

$$H_{\mathrm{AF6}} = +32J_2 - 32J_3 + 32J_5 + 32J_6. \quad (4)$$

Thus, by mapping the relative energies of the seven states obtained from the GGA+U calculations onto the corresponding energies obtained from the total spin-exchange energies, we obtain the values of J_1-J_6 summarized in Table II.

Table II shows that the three major spin-exchange interactions are the nearest-neighbor (NN) intrachain exchange J_1, the NN interchain exchange J_3, and the next-nearest-neighbor (NNN) interchain exchange J_4 in the ab plane. These exchanges do not switch their signs, as the U value changes in the GGA+U calculations. The NNN intrachain spin exchange J_2 and the NN interlayer spin exchanges J_5 and J_6 are weak, and their signs are affected by the value of U. To a first approximation, the spin lattice of Ag_2MnO_2 is described by the three dominant exchanges J_1, J_3, and J_4. The spin exchange J_1 forms one-dimensional antiferromagnetic chains along the b direction. The NN interchain coupling J_3 is frustrating interactions while the NNN ferromagnetic coupling J_4 is not. The strong antiferromagnetic J_1 and ferromagnetic J_4 seem to stabilize the observed magnetic structure at low temperature shown in Fig. 5(c). The quasi-one-dimensional nature of the short-range correlations ($\xi_b \gg \xi_a$) determined from the asymmetric $\frac{d\sigma_{el}}{d\Omega}(\boldsymbol{Q})$ comes from the fact that $|J_3|<|J_1|$ and that J_3 is frustrating. The interlayer spacing is large and the interlayer exchanges J_5 and J_6 differ in sign so that the spin exchanges in the (J_1,J_6,J_6) and (J_3,J_5,J_6) triangles, which form between adjacent triangular layers, are frustrated [see Fig. 5(b) and Table II]. This explains the negligible out-of-plane correlation length of $\xi_c=1.6(16)$ Å.

The collinear spin order of Ag_2MnO_2 seen from our neutron-scattering measurement is explained by considering the effect of spin-orbit coupling (SOC) in each axially elongated MnO_6 octahedron. The $3d$ states of the Mn^{3+} ion at each MnO_6 octahedron are split as $(xz,yz)^2<(xy)^1<(z^2)^1<(x^2-y^2)^0$, where the local Cartesian z axis is taken along the elongated O-Mn-O bonds, as observed in $TbMnO_3$.[18] Thus, the most important energy gain associated with the SOC interaction between the filled and empty up-spin Mn $3d$ states is given by $\langle xy|\hat{H}_{soc}|x^2-y^2\rangle^2/\Delta E$, where ΔE is the energy difference between the xy and x^2-y^2 states. Since these two have the same m_l values, the maximum energy gain occurs when the spins are oriented along the elongated Mn-O bonds as shown in Fig. 3(b). This SOC effect plus the ferro-orbital ordering of the Mn $3d$ states in Ag_2MnO_2 leads to the observed collinear spin structure. However, Ag_2MnO_2 is prevented from having LRO due to the spin frustration in the NN intrachain and the interlayer spin exchanges.

D. Electronic structure and transport properties

To account for the electrical property of Ag_2MnO_2, we examine the electronic structure of Ag_2MnO_2 on the basis of GGA+U calculations with $U=2.5$ eV. Similar results were obtained with $U=4.5$ eV. Figure 7 summarizes the electronic structure of the ordered spin state of Ag_2MnO_2 [depicted in Fig. 5(c)] in terms of density of states (DOS) and charge-density plots. The total DOS plot of Fig. 7(a) shows the presence of partially filled bands at the Fermi level. In the projected DOS (PDOS) plot calculated for one up-spin Mn site, shown in Fig. 7(b), the occupation of the up-and the down-spin Mn $3d$ states is consistent with the assignment of high-spin Mn^{3+} in Ag_2MnO_2. The PDOS plots around the Fermi level, presented in Fig. 7(c), show that the states around the Fermi level have substantial contributions from the Mn $3d$ and O $2p$ states, and this is also clear from the electron-density plot associated with the states at the Fermi level presented in Fig. 7(d). (In comparing the relative contributions of a diffuse orbital such as the Ag $5s$ orbital and a contracted orbital such as the Mn $3d$ or the O $2p$ orbital in terms of charge-density and PDOS plots, one should note that the contribution of the diffuse orbital appears smaller than that of the contracted orbital even if they contribute equally to the state.) Furthermore, the Mn $3d$ and O $2p$ states at the Fermi level are strongly spin polarized. Consequently, electron-electron scattering should dominate over electron-phonon scattering at low temperatures, which may lead to the observed $\rho \propto T^2$ behavior with a large coefficient, A, below 50 K.[4] The presence of the Mn orbital at the Fermi level has recently been observed by a x-ray spectroscopy study.[19]

IV. CONCLUDING REMARKS

Our neutron-diffraction/scattering measurements show that the Jahn-Teller active Mn^{3+} ions of Ag_2MnO_2 adopt a

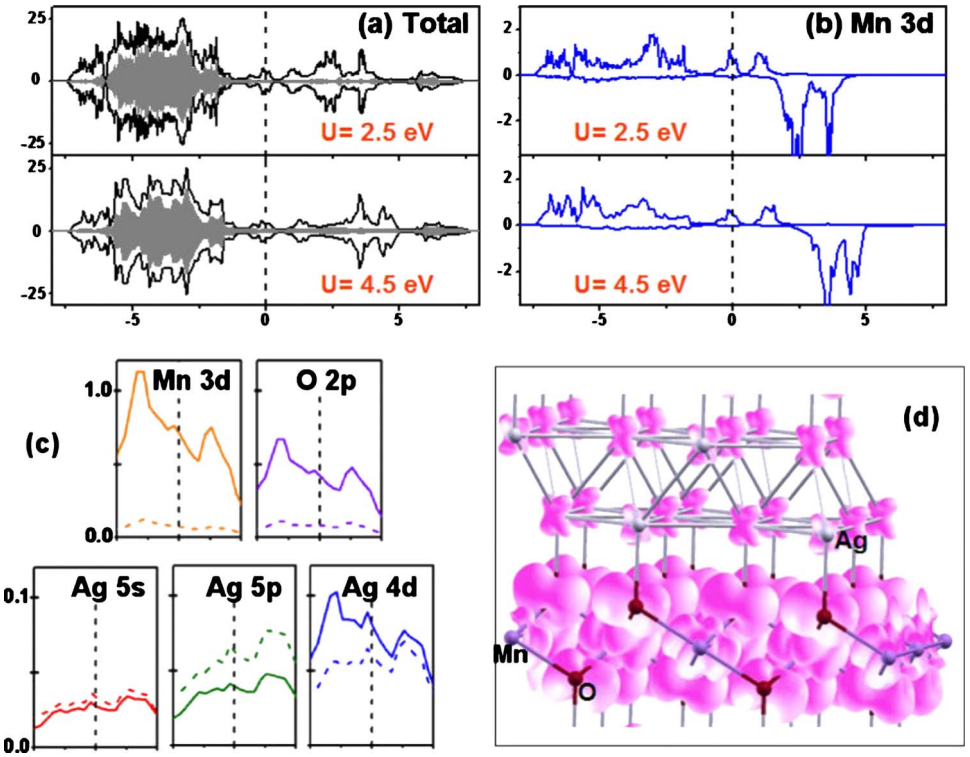

FIG. 7. (Color online) The electronic structure of the ordered spin state [Figs. 1(c) and 5(c)] of Ag_2MnO_2 obtained from GGA+U calculations. All the results shown were obtained with U=2.5 eV except the ones with U=4.5 eV shown in the lower panels in (a) and (b). (a) The total DOS (black line) and PDOS of the Ag atoms (gray shading) in number of states/eV/4 formula units as a function of energy in electron volt. The up- and down-spin DOS are represented by plus and minus numbers, respectively. (b) The PDOS of the Mn 3d states calculated for one up-spin Mn site. (c) The PDOS calculated for the Mn 3d, O 2p, Ag 5s, Ag 5p, and Ag 4d states around the Fermi level. The horizontal axis covers the energy from −0.2 to +0.2 eV. The up- and down-spin DOS plots are represented by solid and dashed curves, respectively. (d) The charge-density distribution associated with the Fermi level, obtained by considering the occupied and unoccupied states lying within 0.01 eV from the Fermi level.

ferro-orbital ordering and the spins of the Mn^{3+} ions freeze into a gapless short-range collinear state below 50 K. Our neutron-scattering experiments show that the spin-spin correlation lengths decrease in the order, $\xi_b \gg \xi_a \gg \xi_c$, which is explained by the spin exchanges calculated for the ferro-orbital ordered state. The states around the Fermi level have significant contributions from the spin-polarized Mn 3d and O 2p states, which makes electron-electron scattering dominate over electron-phonon scattering at low temperatures leading to the $\rho \propto T^2$ behavior with a large coefficient, A, below 50 K.

ACKNOWLEDGMENTS

The work at University of Virginia and NCNR were supported by NSF under Agreements No. DMR-0903977 and No. DMR-0454672, respectively. M.H.W. thanks U.S. Department of Energy for financial support (Grant No. DE-FG02-86ER45259) and computer resources at the NERSC Center and the HPC Center of NCSU. S.H.L. thanks the WPI-Advanced Institute for Materials Research at Tohoku University for their hospitality during his stay when this paper was partially written.

*shlee@virginia.edu

[1] J. G. Bednorz and K. A. Muller, Z. Phys. B: Condens. Matter **64**, 189 (1986).

[2] Y. Kamihara, T. Watanabe, M. Hirano, and H. Hosono, J. Am. Chem. Soc. **130**, 3296 (2008).

[3] H. Yoshida, Y. Muraoka, T. Sorgel, M. Jansen, and Z. Hiroi, Phys. Rev. B **73**, 020408(R) (2006).

[4] H. Yoshida, S. Ahlert, M. Jansen, Y. Okamoto, J.-I. Yamaura, and Z. Hiroi, J. Phys. Soc. Jpn. **77**, 074719 (2008).

[5] J. Rodríguez-Carvajal, Physica B **192**, 55 (1993).

[6] P. E. Blöchl, Phys. Rev. B **50**, 17953 (1994).

[7] G. Kresse and J. Hafner, Phys. Rev. B **49**, 14251 (1994).

[8] G. Kresse and J. Furthmüller, Comput. Mater. Sci. **6**, 15 (1996).

[9] J. P. Perdew, J. A. Chevary, S. H. Vosko, K. A. Jackson, M. R. Pederson, D. J. Singh, and C. Fiolhais, Phys. Rev. B **46**, 6671 (1992).

[10] S. L. Dudarev, G. A. Botton, S. Y. Savrasov, C. J. Humphreys, and A. P. Sutton, Phys. Rev. B **57**, 1505 (1998).
[11] J. A. Mydosh, *Spin Glasses* (Taylor and Francis, London, 1993).
[12] S.-H. Lee, C. Broholm, G. Aeppli, A. P. Ramirez, T. G. Perring, C. J. Carlile, M. Adams, T. J. L. Jones, and B. Hessen, Europhys. Lett. **35**, 127 (1996).
[13] J. Sugiyama, H. Nozaki, Y. Ikedo, K. Mukai, P. L. Russo, D. Andreica, A. Amato, H. Yoshida, and Z. Hiroi, Phys. Rev. B **78**, 104427 (2008).
[14] I. A. Zaliznyak and S.-H. Lee, *Neutron Scattering with 3-Axis Spectrometer* in Modern Techniques for Characterizing Magnetic Materials, edited by Y. Zhu (Kluwer, Boston/Dordrecht/London, 2004).
[15] S.-H. Lee, C. Broholm, G. Aeppli, T. G. Perring, B. Hessen, and A. Taylor, Phys. Rev. Lett. **76**, 4424 (1996).
[16] D. Dai and M.-H. Whangbo, J. Chem. Phys. **114**, 2887 (2001).
[17] D. Dai and M.-H. Whangbo, J. Chem. Phys. **118**, 29 (2003).
[18] H. J. Xiang, S.-H. Wei, M.-H. Whangbo, and J. L. F. Da Silva, Phys. Rev. Lett. **101**, 037209 (2008).
[19] R. Eguchi, H. Yoshida, Y. Okamoto, A. Chainani, M. Matsunami, Y. Ishida, M. Oura, Y. Senba, H. Ohashi, S. Shin, and Z. Hiroi, J. Phys. Soc. Jpn. **79**, 023704 (2010).